

Wearable Triboelectric–Human–Machine Interface (THMI) Using Robust Nanophotonic Readout

Bowei Dong,[#] Yanqin Yang,[#] Qiongfeng Shi,[#] Siyu Xu, Zhongda Sun, Shiyang Zhu, Zixuan Zhang, Dim-Lee Kwong, Guangya Zhou, Kah-Wee Ang, and Chengkuo Lee*

Cite This: *ACS Nano* 2020, 14, 8915–8930

Read Online

ACCESS |

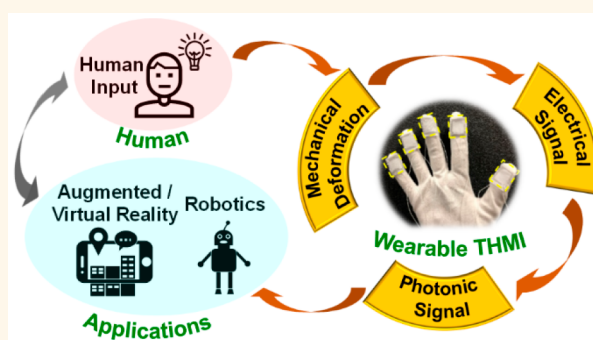
Metrics & More

Article Recommendations

Supporting Information

ABSTRACT: With the rapid advances in wearable electronics and photonics, self-sustainable wearable systems are desired to increase service life and reduce maintenance frequency. Triboelectric technology stands out as a promising versatile technology due to its flexibility, self-sustainability, broad material availability, low cost, and good scalability. Various triboelectric–human–machine interfaces (THMIs) have been developed including interactive gloves, eye blinking/body motion-triggered interfaces, voice/breath monitors, and self-induced wireless interfaces. Nonetheless, THMIs conventionally use electrical readout and produce pulse-like signals due to the transient charge flows, leading to unstable and lossy transfer of interaction information. To address this issue, we propose a strategy by equipping THMIs with robust nanophotonic aluminum nitride (AlN) modulators for readout. The electrically capacitive nature of AlN modulators enables THMIs to work in the open-circuit condition with negligible charge flows. Meanwhile, the interaction information is transduced from THMIs' voltage to AlN modulators' optical output *via* the electro-optic Pockels effect. Thanks to the negligible charge flow and the high-speed optical information carrier, stable, information-lossless, and real-time THMIs are achieved. Leveraging the design flexibility of THMIs and nanophotonic readout circuits, various linear sensitivities independent of force speeds are achieved in different interaction force ranges. Toward practical applications, we develop a smart glove to realize continuous real-time robotics control and virtual/augmented reality interaction. Our work demonstrates a generic approach for developing self-sustainable HMIs with stable, information-lossless, and real-time features for wearable systems.

KEYWORDS: triboelectric nanogenerator, human–machine interface, nanophotonics readout, smart glove, real-time interaction



Wearable electronics has rapidly advanced over the past decade toward conformal, flexible, and stretchable devices for personalized healthcare,^{1,2} smart displays,^{3,4} robotics,^{5,6} Internet-of-Things (IoT),⁷ and diversified applications.⁸ Meanwhile, wearable photonics has been developed as a complementary technology that brings about two major benefits, namely, radio frequency interference (RFI)-free sensing⁹ and high-speed data transmission capability.¹⁰ Several wearable electronic and photonic building blocks have been investigated including flexible physical sensors,¹¹ biochemical sensors,¹² cameras,¹³ waveguides,¹⁴ light-emitting devices,^{15,16} and photodetectors.¹⁷ In the era of IoT and fifth-generation (5G) wireless networks, numerous widely distributed devices including wearable electronics/ photonics are expected to be interconnected wirelessly with ultrafast data exchange rates, providing real-time communication between ambient information and human information to

enable the desired interactions and interventions.^{18,19} Accordingly, a body area sensor network (bodyNET) was achieved by hybridizing a huge number of wearable devices on human bodies with potential applications for personalized healthcare and multifunctional robotics.²⁰ As the high power consumption imposed by the tremendous wearable devices limits the duration of use and requires frequent maintenance, independent and self-sustainable wearable systems are desired

Received: May 5, 2020
Accepted: June 23, 2020
Published: June 23, 2020



for implantable devices and crucial remote security/safety monitoring.

To realize self-sustainable systems, integrating wearable electronics/photronics with rapidly developing energy harvesting and storage technologies has been considered as a promising solution.^{21–27} Individual or hybrid energy harvesting technologies (e.g., piezoelectric, electromagnetic, thermoelectric, pyroelectric, and triboelectric mechanism) can be incorporated into the wearable systems in two common forms, i.e., energy harvesters^{28–31} and self-sustainable sensors.^{32,33} Energy harvesters can scavenge the ambient available energy and convert it into electricity, which can be stored in the energy storage units to support the sustainable operation of the whole wearable systems.^{34–39} On the other hand, self-sustainable sensors with self-generated electrical signals in response to external stimuli can greatly reduce the overall energy consumption in the wearable systems.^{40–44}

Since the first invention of the triboelectric nanogenerator (TENG), triboelectric devices have shown great potential applications in self-sustainable wearable electronics/photronics and thereby received tremendous development, due to the superior advantages in high-output performance, flexible/stretchable compatibility, widely available materials, low cost, simple fabrication, and high scalability.^{45–59} Briefly speaking, the operation mechanism of the TENG is based on the coupling of contact electrification and electrostatic induction of two dissimilar triboelectric materials, thus driving electrons to flow in external circuits and producing electrical signals accordingly.^{60–62} Recently, TENG research interests have gradually migrated to three major aspects, namely, triboelectric materials with specific functionalities,^{63–65} self-sustainable triboelectric–human–machine interface (THMI) for IoT applications,^{66,67} and THMIs for robotic control and virtual/augmented reality (VR/AR) interactions.^{68–70} In terms of the developed THMIs, diversified wearable configurations have been explored to enhance user experience and convenience for a broad range of human interactions. The widely investigated configurations include finger-bending sensors,⁷¹ interactive gloves,⁷² tactile sensors,⁷³ eye blinking/body motion-triggered interfaces,^{74,75} voice/breath monitors,^{76,77} and self-induced wireless sensors.⁷⁸ Nonetheless, a major restriction of THMIs is their pulse-like signals, which are unstable and even cause stimuli information loss.^{79,80} The pulse-like signal is a practical limitation when THMIs are connected to external circuits. Due to the transient current flow upon the electrostatic induction process, the THMI's electrical states determined by different stimuli shift rapidly to the electrostatic equilibrium, resulting in only a sharp pulse-like signal received by the external readout circuit with significant information loss. One solution is to use a high-impedance readout circuit to suppress current flows as well as the corresponding electrical state shifts.^{81,82} Yet, an amplifying circuit is required to read the small current information, complicating the sensing system. Another solution involves the utilization of deep learning techniques.^{83–86} By training the deep neural network (DNN) with abundant data, the DNN can extract the major features of the pulse-like signal and make correct decisions even in the presence of information loss. Nonetheless, the deep learning techniques require massive training data and large computation power.⁸⁷

Here, we propose a THMI using robust nanophotonic readout that suppresses the electrical state shift to enable stable, information-lossless, and real-time human–machine interactions. The THMI's output is applied to a nanophotonic

aluminum nitride (AlN) Mach–Zehnder interferometer (MZI) modulator composed of a micro parallel-plate capacitor sandwiching an AlN MZI. While the THMI works in the open-circuit condition with negligible current flows so that its electrical state determined by different stimuli can be maintained, the optical transmission in the AlN MZI is changed by the applied open-circuit voltage (V_{oc}) according to the electro-optic Pockels effect. An additional advantage enabled by the nanophotonic readout is the real-time monitoring capability thanks to the high data transmission rate. Leveraging the design flexibility of THMIs, various linear force sensitivities in different ranges are achieved by properly designing the THMI and the corresponding nanophotonic readout circuit. Notably, thanks to the open-circuit working condition enabled by the nanophotonic readout, force sensitivities are independent of the force speed, providing an indispensably good property for practical applications. As a proof-of-concept, we demonstrate a smart glove for continuous real-time robotic hand control and VR/AR interactions. Moving forward, the proposed approach featuring the utilization of nanophotonics for triboelectric technology serves as a versatile method to develop self-sustainable devices with stable, information-lossless, and real-time monitoring capability for wearable electronics applications.

RESULTS AND DISCUSSION

Figure 1 depicts the conversion between physical quantities and the related physical effects that enable the information flow in the wearable THMI–nanophotonics system. The human inputs a force signal (F), causing a mechanical deformation (Δx) in the THMI according to the stress–strain relation. The mechanical deformation is transduced to an

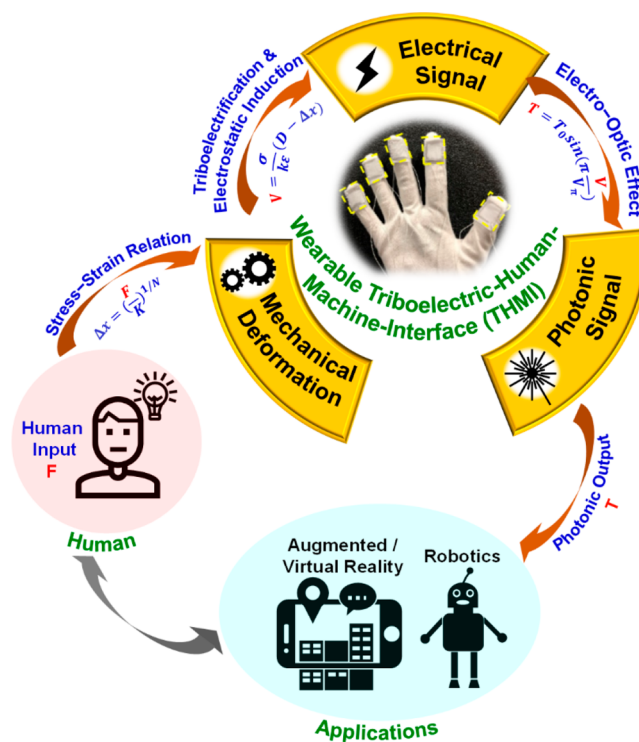


Figure 1. Concept of wearable THMI–nanophotonics systems. The conversion between physical quantities and the related physical effects enabling the interaction information flow.

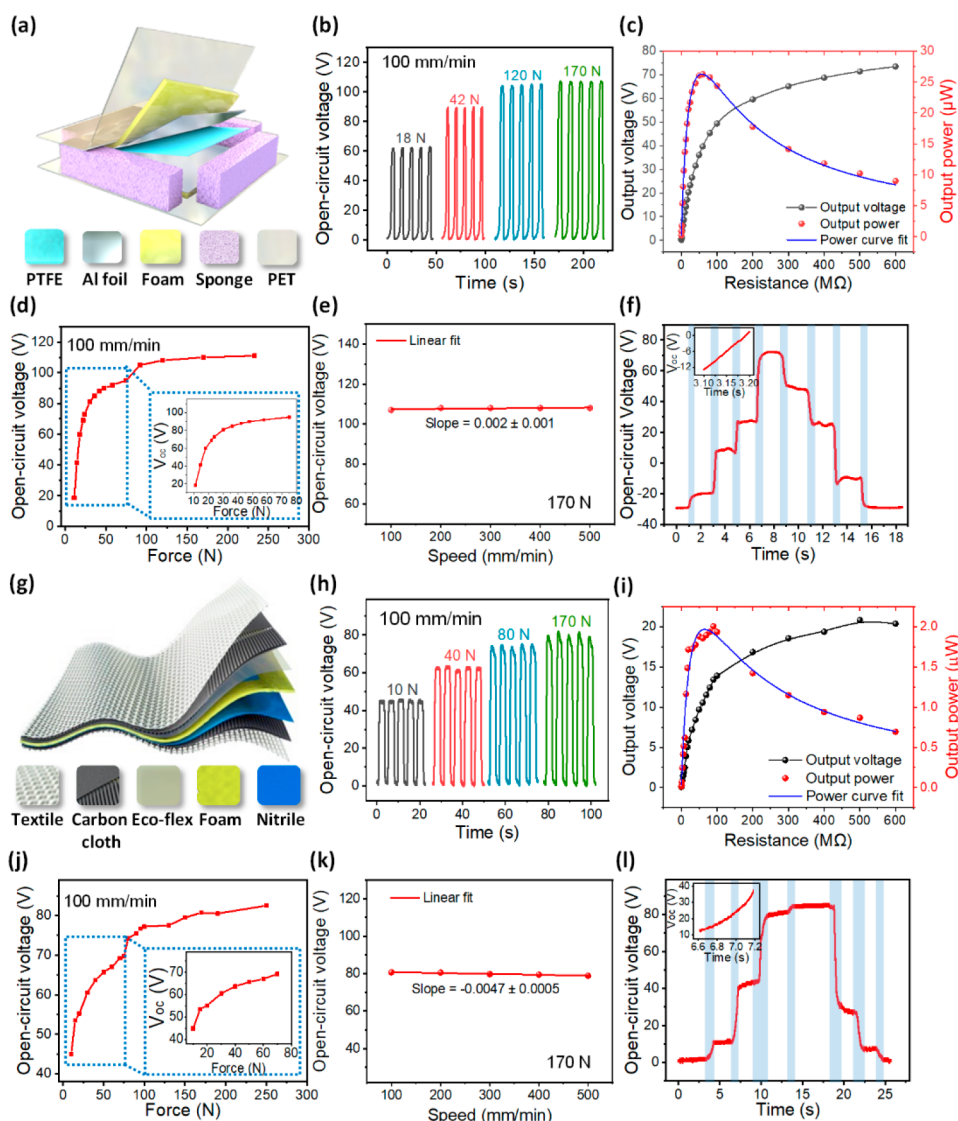


Figure 2. Characteristics of two triboelectric–human–machine interfaces (THMIs) that cover different interaction force ranges. (a–f) Spacer THMI (S-THMI). (a) Schematic illustration. (b) Open-circuit voltage (V_{oc}) stimulated by a force gauge with four different applied F at the same moving speed (v_F) of 100 mm/min. (c) Output power (P) under 170 N at 100 mm/min when connected with different external resistances (R'). (d) Relation between V_{oc} and F at a constant v_F . (e) V_{oc} under five different v_F 's at 170 N. (f) Electrical state stability test proved by the steady V_{oc} at different values in one contact/separation cycle controlled by the human hand. (g–l) Textile THMI (T-THMI). (g) Schematic illustration. (h) V_{oc} under four different F 's at 100 mm/min. (i) P under 170 N at 100 mm/min when connected with different R 's. (j) Relation between V_{oc} and F at constant v_F . (k) V_{oc} under five different v_F 's at 170 N. (l) Electrical state stability test.

electrical signal (V) through the triboelectrification and electrostatic induction process. The electrical signal is then applied to the nanophotonic readout circuit and transduced into a photonic signal (T) by the electro-optic Pockels effect. The photonic signal is finally read out for human–machine interactions. A schematic showing the general working mechanism of the integrated system is provided in Note S1.

To cover different application aspects in human–machine interactions, interaction forces covering different ranges are required. Accordingly, we develop two wearable THMI–nanophotonics systems. One system has a spacer THMI (S-THMI) integrated with a short AlN MZI modulator. The other one has a textile THMI (T-THMI) integrated with a long AlN MZI modulator. The images of the four individual devices for the two THMIs are shown in Note S2, and their characteristics are investigated individually in Figure 2 and Figure 3. As indicated in Figure 2a, the S-THMI is composed

of a negative triboelectric part of PTFE/Al/foam/PET and a positive triboelectric part of Al/foam/PET, with a sponge spacer in between. After fabrication, the S-THMI is characterized using a force gauge testing system that applies forces with controllable magnitudes (F) and speeds (v_F). The measured V_{oc} of S-THMI under different F 's of 18, 42, 80, and 170 N (at a constant v_F of 100 mm/min) are shown in Figure 2b, where V_{oc} is positively related to F . The output voltage (V) and power (P) performance of the S-THMI at different external resistances (R') is also measured (Figure 2c), with an F of 170 N and v_F of 100 mm/min. According to the fitting curve (details in Note S3), it can be observed that while V keeps increasing, P first increases and then decreases with R' , exhibiting the maximum value of 26.3 μ W at a matched R' of 57.3 M Ω . The detailed force response of V_{oc} is characterized under different F 's and v_F 's. From Figure 2d, the V_{oc} of S-THMI rapidly increases from 19 V at 10 N to 81 V at 30 N,

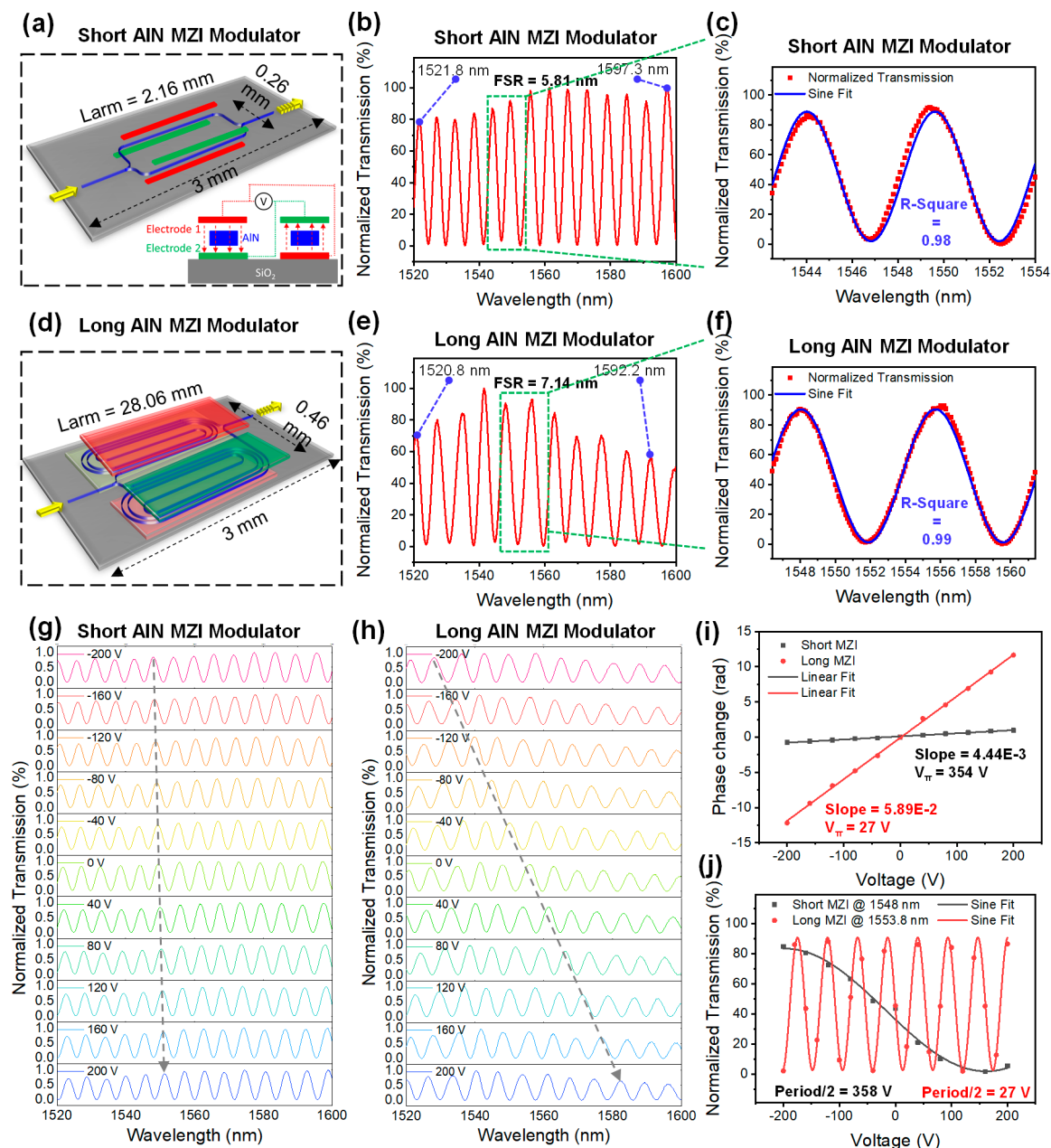


Figure 3. Wavelength spectrum and direct-current (DC) characteristics of AlN MZI modulators. (a) Schematic of the short AlN MZI modulator. (b) Short MZI wavelength spectrum in the telecommunication wavelength range of 1520–1600 nm. (c) Zoom-in of (b) to 1548 nm with a sine fit. (d) Schematic of the long AlN MZI modulator. (e) Long AlN MZI modulator wavelength spectrum. (f) Zoom-in of (e) to 1554 nm with sine fit. (g and h) DC characteristics of (g) the short and (h) the long AlN MZI modulator. (i) Relation between phase change and applied voltage extracted from (g) and (h). (j) Relation between T and V extracted from (g) and (h).

then slowly rises to 92 V at 60 N and saturates thereafter (>60 N). On the other hand, V_{oc} is not affected by v_F from 100 mm/min to 500 mm/min as implied by the near-zero linearly fitted slope, showing good stability across different v_F 's (Figure 2e). Since V_{oc} is solely determined by F and independent of v_F , it can be adopted as the output indicator for real-time force monitoring. As further illustrated in Figure 2f, V_{oc} can practically respond exactly to the force profile induced by hand control, fully reflecting the force information. It is also noteworthy that V_{oc} can be maintained at different levels, which is an important characteristic of THMIs working in the open-circuit condition.

In addition to the S-THMI, another THMI fabricated by textile materials, *i.e.*, textile THMI (T-THMI), is developed to achieve a larger interaction force range (Figure 2g). The T-THMI is composed of a negative Ecoflex-coated conductive carbon cloth, a narrow-gap spacer, and a positive nitrile layer with another carbon cloth, encapsulated by two pieces of nonconductive textiles for electrical insulation. The testing results of the T-THMI under different F 's of 10, 40, 80, and 170 N (at a constant v_F of 100 mm/min) are illustrated in Figure 2h, indicating a positive relation between V_{oc} and F as well. Based on the V and P performance of the T-THMI at different R 's (Figure 2i), the maximum P of 1.97 μ W can be achieved at a matched R' of 65.4 M Ω (details in Note S3). As

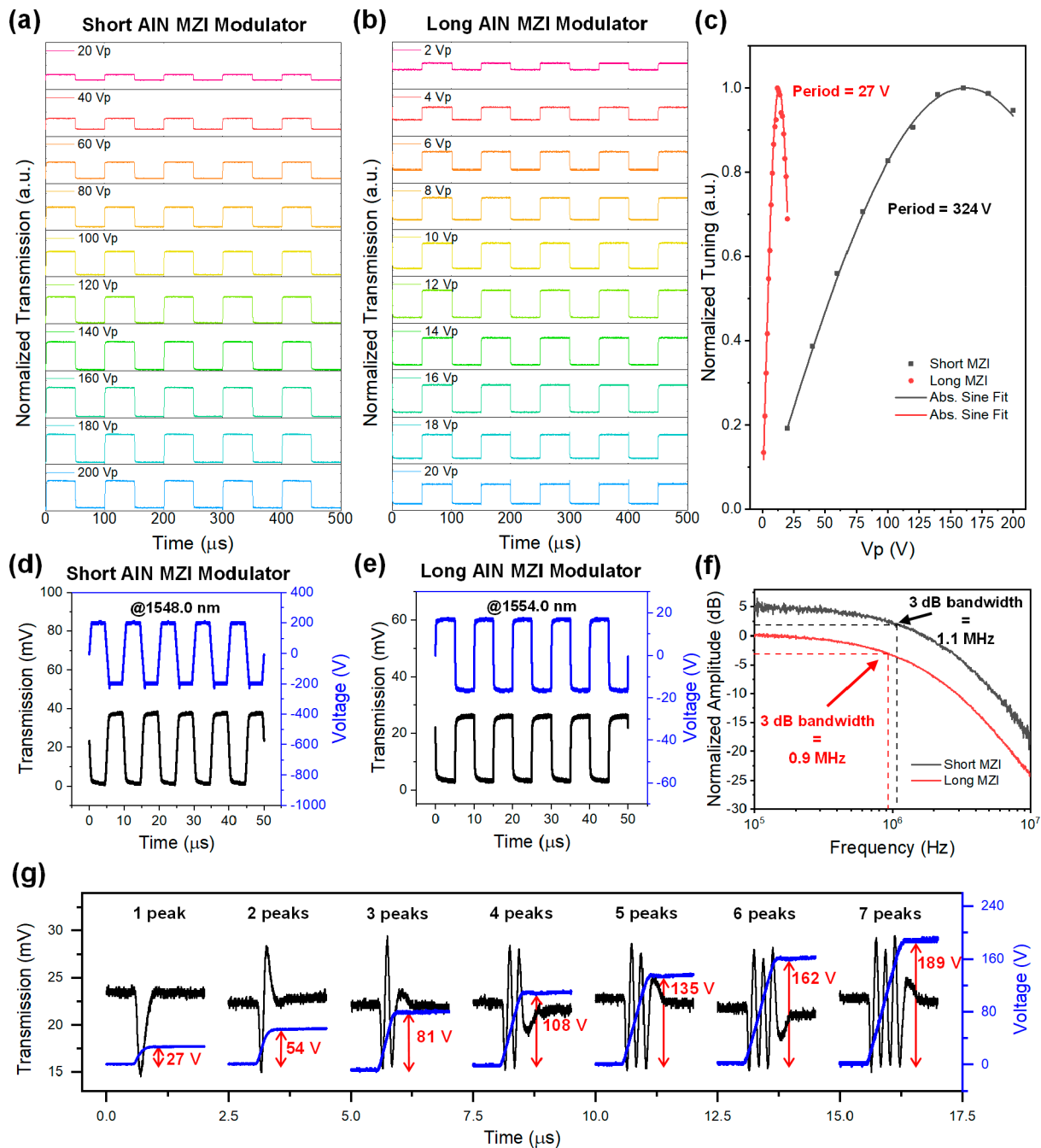


Figure 4. Alternating current (AC) characteristics of AlN MZI modulators. (a and b) AC responses of (a) the short and (b) the long AlN MZI modulator. (c) Relation between the normalized tuning and the applied V_p extracted from (a) and (b). The “normalized tuning” is defined as the opening of the modulated optical transmission, *i.e.*, the difference between the highest and lowest transmission level. (d and e) Temporal spectra of the modulated optical transmission at 10 kHz. The nanophotonic readout circuits can preserve the full information on the voltage waveform. (f) 3 dB bandwidth measurement of the AlN MZI modulators. (g) Temporal T response of the long AlN MZI modulators at high voltage.

shown in Figure 2j, V_{oc} of the T-THMI gradually increases from 45 V at 10 N to 77 V at 115 N, after which V_{oc} becomes relatively stable. Compared with the S-THMI, the force sensitive range is extended from 60 to 115 N, but V and P are both smaller. In terms of the effect of different v_F 's, V_{oc} of T-THMI is also consistent under different v_F 's from 100 mm/min to 500 mm/min (Figure 2k). According to the V_{oc} profile generated by human hand control as shown in Figure 2l, it is confirmed that V_{oc} can be precisely controlled as well.

After the investigation of individual THMIs, AlN MZI modulators are characterized to ensure that they can carry the THMIs' voltage signals effectively. A short and a long AlN MZI modulator are designed to integrate with the S-THMI and the T-THMI, respectively. Although the T-THMI's saturation force is larger, its V_{oc} is lower. Thus, a longer AlN MZI modulator is required to provide a strong electric-field (E-field)–light interaction for maintaining a high nanophotonic readout resolution. The short AlN MZI modulator with the arm length of $L_{arm} = 2.16$ mm occupies a footprint of only 0.81

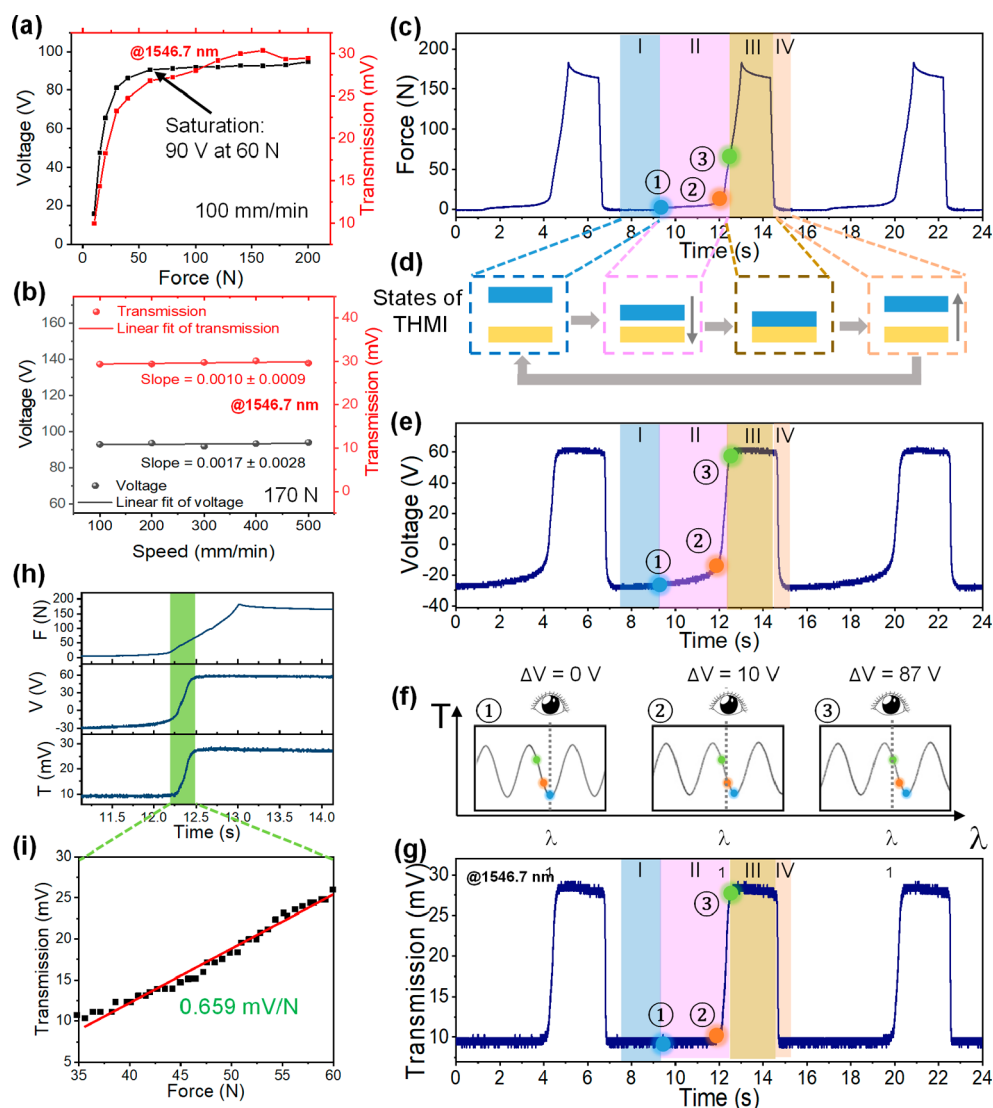


Figure 5. Characteristics and working principle of the wearable S-THMI using nanophotonics readout. (a and b) Output characteristics of the integrated system, S-THMI's output voltage (V_{S-THMI}), and the corresponding T , (a) under various F 's at 100 mm/min, (b) under five different v_F 's at 170 N. (c–g) Working mechanism of the integrated system operating at an MZI destructive interference trough: (c) temporal F spectrum, (d) S-THMI's states corresponding to different force stages shaded in (c), (e) temporal S-THMI's V spectrum, (f) sketch of the MZI interference spectrum corresponding to three critical force states labeled in (c), (g) temporal T spectrum. (h) Zoom-in of (c), (e), and (g) to 11–14 s for the analysis of the detailed relation between F , V_{S-THMI} , and T . (i) Linear relation between T and F in the 35–60 N force range with a sensitivity of 0.659 mV/N.

mm² (Figure 3a). The top and bottom electrodes sandwich the AlN waveguide. To double the effective EO tuning efficiency, the electrodes are connected using the push–pull configuration as shown in the inset of Figure 3a; that is, the top (bottom) electrode of one arm serves as the bottom (top) electrode of the other arm. A free-spectral range (FSR) of 5.81 nm in the telecommunication wavelength range of 1520 to 1600 nm is presented in Figure 3b. The zoom-in wavelength spectrum in Figure 3c shows a sine fit with an R -square of 0.98, illustrating the high quality of the short AlN MZI modulator, whose optical transmission (T) is theoretically governed by interference. Correspondingly, the schematic of the long AlN MZI modulator with $L_{arm} = 28.06$ mm and a footprint of 1.8 mm² is shown in Figure 3d, while an FSR of 7.14 nm and a sine fit with an R -square of 0.99 are presented in Figure 3e and f, respectively. It is worth noting that nontrivial transmission variation can be observed in Figure 3e to affect sine fit since

the fitted amplitude should be a unique value. However, this problem can be tackled by a more sophisticated interferogram fitting method presented in Note S4.

Next, we investigate the direct current (DC) tuning characteristics of both AlN MZI modulators. When the voltage bias (V) applied on the MZI modulator increases from -200 V to 200 V, a constructive interference peak shifts by 3.2 and 54.2 nm in the short (Figure 3g) and the long AlN MZI modulator (Figure 3h), respectively. The dependence of the phase change on V is illustrated in Figure 3i. V 's required for a π -phase shift (V_π) are 354 and 27 V in the short and the long AlN MZI modulator, respectively. Using the V -dependent temporal T spectrum in Figure 3g and h, we construct the T – V curve and plot it in Figure 3j. In the short AlN MZI modulator at 1548 nm, T almost changes monotonically as V varies monotonically from -200 to 200 V. On the contrary, in the long AlN MZI modulator at 1553.8 nm, T changes

periodically under a similar applied V . The higher voltage sensitivity of the long AlN MZI modulator can be attributed to its longer L_{arm} that provides a stronger E-field–light interaction. We adopt a sine fit for Figure 3j and obtain a period of 716 and 54 V in the short and the long AlN MZI modulator, respectively, corresponding to their V_{π} values of 358 and 27 V. The two V_{π} values are consistent with the V_{π} values extracted from Figure 3i. Quantitatively, the ratio of the V_{π} values is 13.11, while the ratio of the two L_{arm} 's is 12.99. The two close ratios reveal the proportionality between phase change and L_{arm} under DC biases. The proportionality is further analyzed and confirmed by a theoretical analysis in Note S5.

After the investigation of DC characteristics of the AlN MZI modulators, we study the alternating current (AC) characteristics. Figure 4a and b present the temporal spectrum of normalized T in the short and the long AlN MZI modulator, respectively, under 10 kHz AC square-wave modulation signal with different peak voltage (V_p). The term “normalized tuning” is defined as the opening of the temporal spectrum of the modulated T , *i.e.*, the difference between the high and the low T value. In the short AlN MZI modulator, the normalized tuning gradually increases when V_p rises from 20 V to 160 V in steps of 20 V, after which the normalized tuning almost saturates. A different behavior is observed in the long AlN MZI modulator, where the normalized tuning rises to the maximum at 12 V_p , then drops as V_p further increases. The quantitative relation between normalized tuning and V_p is plotted in Figure 4c. The data points are extracted from Figure 4a and b. Absolute sine functions are employed for fitting since the normalized tuning cannot be negative. Fitted periods of 324 and 27 V in the short and the long AlN MZI modulator, respectively, are revealed with R -squares higher than 0.99 for both conditions. The agreement in fitted periods in the case of DC and AC tuning suggests the speed of MZIs is faster than 10 kHz. The temporal T responses of the short and the long MZI under 100 kHz AC modulation are plotted in Figure 4d and e, respectively. The optical waveforms can reproduce the voltage waveforms, demonstrating the effective transduction from electrical signal to photonic signal using the AlN MZI modulators at a 100 kHz data transmission rate. To further understand the AlN MZI modulators' speed limit, we implement a 3 dB measurement using a vector network analyzer (VNA). The measured results shown in Figure 4f indicate a 3 dB bandwidth of 0.9 MHz in the long AlN MZI modulator and 1.1 MHz in the short AlN MZI modulator. The black curve has been moved up by 5 dB manually for visual clarity. In particular, the ~ 1 MHz modulation speed achieved in both AlN MZI modulators allows nanophotonic readout circuits to capture THMIs' signals with a temporal resolution of around 1 μs , which can satisfy most of the applications related to human/machine interactions. An interesting difference between the temporal T spectrum of the short and the long AlN MZI modulators under high AC voltages ($V_p > 13.5$ V) is their distinct behaviors at waveform edges. As shown in Figure 4d, the temporal T spectrum preserves the features of the input temporal V spectrum even at $V_p = 200$ V in the short AlN MZI modulator. Contrarily, as suggested by Figure 3j, when a square wave voltage is applied to the long AlN MZI modulator, T would experience several oscillations temporally depending on the magnitude of V at the square wave edges. Since the relation between T and V follows a sine function with a period of 54 V, we operate the long AlN MZI modulator at

1553.8 nm, which corresponds to a zero-phase wavelength in its wavelength spectrum (Figure 3f). Consequently, after every π -phase shift, T is expected to cross one peak and return to the same value (Figure 3j). Such behaviors are observed and presented in Figure 4g. A voltage pulse that sharply rises from 0 V to $[27 \times N]$ V is applied to the long MZI, where N is an integer ranging from 1 to 7. It is observed that N peaks appear in the temporal T spectrum when $[27 \times N]$ V is applied, and T finally reaches the same level as T at 0 V. In addition, the observed transmission overshoots right after the voltage stabilization are explained in Note S6.

Theoretically, the integration of THMIs and nanophotonic readout circuits can be conveniently achieved through connecting the two THMI electrodes to the pair of electrodes sandwiching the AlN MZI waveguide. Due to the electrically capacitive nature of the AlN MZI modulator with a very small capacitance, the THMIs work in the open-circuit condition without current flows that render electrical state shifts. The THMI output voltage (V_{THMI}) is applied on the AlN MZI modulators, inducing an E-field across the AlN waveguide to change AlN's refractive index through the electro-optic Pockels effect. In this way, T of AlN MZI carries the information delivered by V_{THMI} since T is governed by the refractive index. To confirm the feasibility of the proposed methodology, we first integrate the S-THMI with the short AlN MZI modulator and explore the characteristics of the integrated system. Figure 5a shows S-THMI's output voltage ($V_{\text{S-THMI}}$) under different F 's at 100 mm/min. The dependence of $V_{\text{S-THMI}}$ on F follows a similar trend to that in Figure 2a. $V_{\text{S-THMI}}$ abruptly increases from 16 V at 10 N to 80 V at 30 N, then gradually rises to 90 V at 60 N, and saturates afterward due to the full activation of surface charges in the triboelectrification process. The resultant T changes correspondingly to $V_{\text{S-THMI}}$. The v_F dependence of $V_{\text{S-THMI}}$ and the corresponding resultant T are presented in Figure 5b. The independence of $V_{\text{S-THMI}}$ on v_F is preserved. The resultant T is also stable, showing the independence of v_F . Figure 5a and b together suggest that S-THMI's characteristics are maintained after its integration with the short AlN MZI modulator. Meanwhile, it is confirmed that the S-THMI is working in the open-circuit condition; otherwise $V_{\text{S-THMI}}$ will show v_F dependence. The detailed working principle of continuous real-time THMI enabled by nanophotonic readout is illustrated in Figure 5c to g. When $V_{\text{S-THMI}}$ is at the lowest, the short AlN MZI modulator is initially working at $\lambda = 1546.7$ nm, which corresponds to a destructive interference with the lowest T . One force cycle is divided into four regions, as illustrated by the color-shaded areas (Figure 5c). The blue region (region I) refers to the zero-force stage where the two triboelectric layers are fully separated. The corresponding electrostatically induced $V_{\text{S-THMI}}$ (-25 V as shown in Figure 5e) maintains the lowest T (10 mV as shown in Figure 5g) in the nanophotonic readout circuit. In the pink region (region II), F is gradually exerted on the S-THMI so that the top triboelectric layer is approaching the bottom one. $V_{\text{S-THMI}}$ increases and leads to the rise of T . The brown region (region III) corresponds to the period when F exceeds the saturation value (60 N as shown in Figure 5a) while the two triboelectric layers are in tight contact. The resultant $V_{\text{S-THMI}}$ remains unchanged (90 V), like T (28 mV). In the orange region (region IV), the two triboelectric layers begin to separate apart from each other when F starts to drop. As F decreases to < 60 N, $V_{\text{S-THMI}}$ and T begin to fall back to the lowest value. In one interaction cycle, the stimulus in the form of F mainly interacts

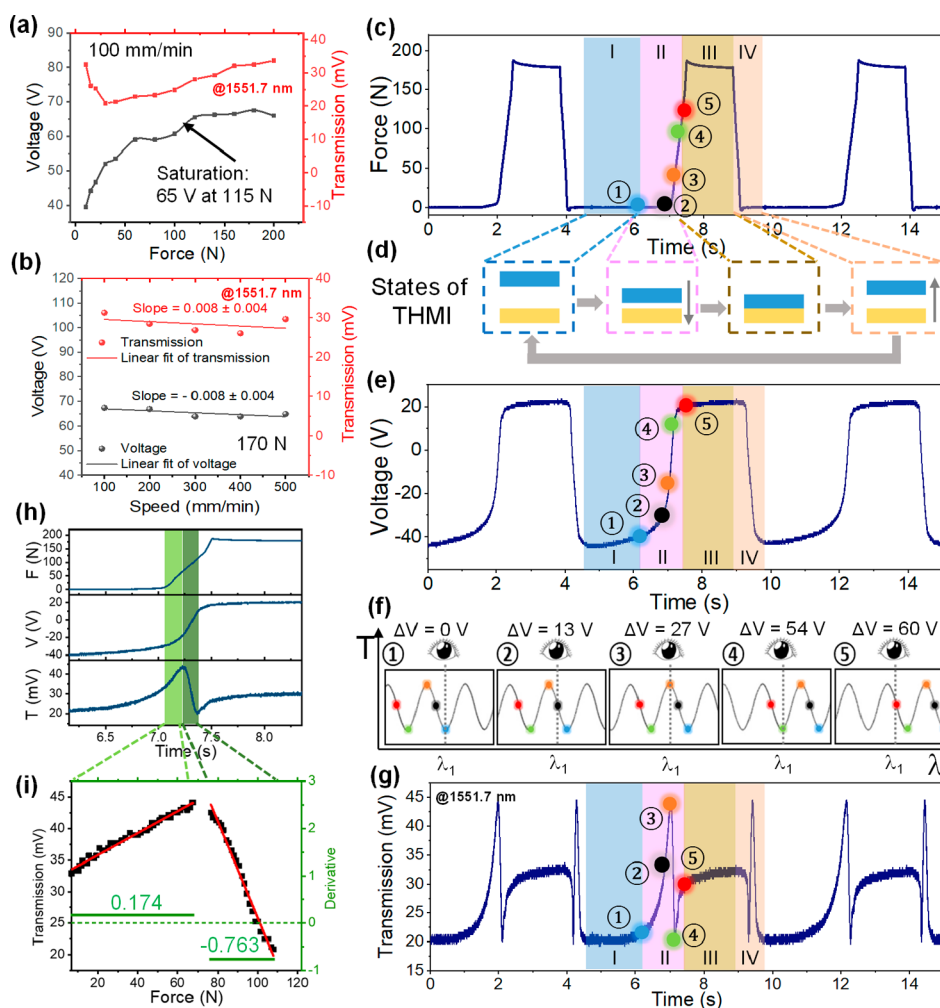


Figure 6. Characteristics and working principle of the T-THMI using nanophotonics readout. (a and b) Output characteristics of the integrated system, T-THMI's output voltage (V_{T-THMI}), and the corresponding T , (a) under various F 's at 100 mm/min, (b) under five different v_F 's at 170 N. (c–g) Working mechanism of the integrated system operating at an MZI destructive interference trough: (c) temporal F spectrum, (d) T-THMIs corresponding to different force stages shaded in (c), (e) temporal V_{T-THMI} spectrum, (f) sketch of the MZI interference spectrum corresponding to five critical force states labeled in (c), (g) temporal T spectrum. (h) Zoom-in of (c), (e), and (g) to 6.0–8.5 s for the analysis of the detailed relation between F , V_{T-THMI} , and T . (i) Linear relation between T and F in the 7–70 N force range with a sensitivity of 0.174 mV/N and the 75–110 N force range with a sensitivity of -0.793 mV/N.

with the wearable S-THMI–nanophotonics system in region II. Thus, region II is further explored in detail. Three critical force states are labeled by ①, ②, and ③, respectively. At state ①, the load cell touches the top surface of the S-THMI and F starts to increase. Between states ① and ②, the two triboelectric layers are pressed toward each other without contact. F increases gradually due to the small elastic coefficient provided by the sponge spacer, causing a slight increase of V_{S-THMI} but a negligible change in T . At state ②, the two triboelectric layers are in contact, so F starts rising due to the abrupt change of the elastic coefficient. The corresponding V_{S-THMI} and T shoot up accordingly. While F increases to the maximum around 190 N, V_{S-THMI} has already saturated at 90 V at state ③ of 60 N, with 27 mV T . Afterward, F is maintained before it drops to 0 N. The temporal V_{S-THMI} and T spectrum follow the same trend. As indicated in Figure 5c to g, T is sensitive between state ② and state ③. Therefore, the zoom-in figure showing the detailed temporal F – V_{S-THMI} – T spectrum in 11–14 s is presented in Figure 5h. The temporal spectra in Figure 5h reveal the relation between F , V_{S-THMI} , and T . The relations

between F , V , and T are theoretically governed by the following set of equations.

Stress–strain relation:

$$\Delta x = \left(\frac{F}{K}\right)^{1/n} \quad (1)$$

Parallel plate capacitor voltage:

$$V = \frac{\sigma}{k\epsilon}(D - \Delta x) + V_C \quad (2)$$

MZI optical transmission:

$$T = T_0 + T' \sin\left(\pi \frac{V - V_0}{V_\pi}\right) \quad (3)$$

where K is the strength coefficient, n is the strain-hardening coefficient, σ is the surface charge density of the triboelectric layer, k is the relative permittivity, which is unity in our case where the dielectric material is air, ϵ is the permittivity, V_C is the initial voltage between the two electrodes in the ambient condition, T_0 is the optical transmission at zero phase, T' is the

amplitude of the oscillating AlN MZI wavelength spectrum, V_0 is related to the initial phase, and V_π is the voltage required for a π -phase shift in the short AlN MZI modulator.

Since the THMI–nanophotonics system reads force information (F) from photonic readout (T), we use the one-to-one corresponding data extracted from Figure 5h to derive the resultant relation between T and F in the S-THMI as

$$T = 8.698 - 18.618 \times \sin \left(\frac{\pi}{358.85} \left[\frac{-19}{34} \left[136 - \left(\frac{F}{5.173} \right)^{1/0.375} \right] - 281 \right] \right) \quad (4)$$

The detailed derivations are shown in Note S7. The data are fitted well by the theoretical model suggested from eq 1 to eq 3, with an R -square of 0.981. In the force range of 35–60 N, T and F are quasi-linearly related (Figure 5i). Hence, we implement linear fitting and obtain a sensitivity of 0.659 mV/N. We leverage the stable, information-lossless, and real-time photonic signal to enable the continuous control of a wireless electronic toy car in real space (Movie S1) and a drone in the VR space (Movie S2). In the wireless electronic toy car control, T is defined to directly regulate the car speed. Notably, during 15–19 s in the movie, the car speed can gradually increase from zero to the maximum. During 28–33 s, the car speed gradually rises to a medium value and is maintained during 33–38 s, showing the successful suppression of electrical state shifts in the S-THMI. After 38 s, the car speed shoots up to the maximum before the speed starts to decrease to zero at 45 s. The practical on-road testing is also demonstrated from 52 s to the end of Movie S1. In the drone control in the VR space, the rate of change of T is defined to directly regulate the drone acceleration. During 7–9 s, a small positive acceleration is introduced to the drone so that its speed rises to a medium value and is maintained until 11 s. At 11 s, a large positive acceleration pulse is introduced to abruptly lift the speed to the maximum. Finally, at 13 and 16 s, two small negative acceleration pulses are introduced to drive the drone to the medium speed and the static state, respectively.

We further leverage the design flexibility of THMIs to extend the applicable interaction force range. As shown in Figure 2j, the T-THMI has a broader interaction force range whose saturation point happens at 115 N instead of only 60 N in the S-THMI. However, the voltage output of the T-THMI ($V_{T\text{-THMI}}$) is lower than $V_{S\text{-THMI}}$. Consequently, the long AlN MZI modulator with higher voltage sensitivity is adopted to be integrated with the T-THMI to compensate for the lower $V_{T\text{-THMI}}$. Like the short AlN MZI modulator, the long one is working at a destructive interference at 1551.7 nm when $V_{T\text{-THMI}}$ is the lowest. Figure 6a presents $V_{T\text{-THMI}}$ and the corresponding T characteristics of the wearable T-THMI–nanophotonics system under different F 's. $V_{T\text{-THMI}}$ gradually increases from 40 V at 10 N to 65 V at 115 N with T falling from 32 mV at 10 N to 20 mV at 40 N and then increasing to 28 mV at 115 N. Figure 6b shows the v_F dependence of $V_{T\text{-THMI}}$ and T . Using linear fitting, straight fitted lines with slopes of -0.008 and 0.008 are derived for $V_{T\text{-THMI}}$ and T , respectively, suggesting that the T-THMI is working in the open-circuit condition. Figure 6c to g explain the working principle of the wearable T-THMI–nanophotonics system. As shown in Figure 6c, one force cycle can be split into four regions with the same definitions as Figure 5c. Region I and region III are similar to Figure 5. Yet, region II and region IV

where the temporal F spectrum shows sharp edges show different features. Interestingly, the temporal T spectrum in these two regions presents oscillations that produce a peak and a trough. To understand the interaction between the stimulus in the form of F and the T-THMI in region II, we identify five characteristic force states, labeled as ①, ②, ③, ④, and ⑤. Before state ①, the load cell is not in contact with the top triboelectric surface so that no force is exerted on the T-THMI. But $V_{T\text{-THMI}}$ and the corresponding T drift slightly due to the dissipation of triboelectrically generated charges to the humid environment (60% relative humidity at room temperature). From state ① to state ②, the top triboelectric layer is pressed toward the bottom one. F mildly increases from 0 to 7 N and $V_{T\text{-THMI}}$ rises from -38 V to -29 V accordingly. Despite the small increment in F and $V_{T\text{-THMI}}$, T is lifted significantly from 22 mV to 33 mV thanks to the long AlN MZI modulator's high voltage sensitivity. At state ②, the two triboelectric layers are in contact, and F starts to rise abruptly. From state ② to state ③, F and $V_{T\text{-THMI}}$ keep increasing until $V_{T\text{-THMI}}$ has increased by 27 V at state ③. At this moment, the long MZI experiences a π -phase shift so the interference changes from destructive to instructive. From states ③ to state ④, F and $V_{T\text{-THMI}}$ increase further until the voltage difference is 54 V at state ④. The long MZI undergoes a 2π -phase shift and the interference returns to be destructive, resulting in the lowest T . Later at state ⑤, F exceeds 115 N, where saturation happens with a $V_{T\text{-THMI}}$ of 65 V, leading to a stable T at around 30 mV afterward. Region IV can be explained similarly to region II. Next, we zoom into region II in 6.0–8.5 s for detailed quantitative analysis. The consolidated temporal spectra in Figure 6h reveal the relation between F , $V_{T\text{-THMI}}$, and T . Extracted from Figure 6h followed by a theoretical analysis, the resultant relation between T and F in T-THMI can be described by eq 5:

$$T = 34.086 + 10.708 \times \sin \left(\frac{\pi}{26.28} \left[-2.434 \left[18.489 - \left(\frac{F - 7}{11.828} \right)^{1/0.769} \right] - 11.4 \right] \right) \quad (5)$$

The detailed derivations are shown in Note S7. The data are fitted well by the theoretical model suggested from eq 1 to eq 3, with an R -square of 0.939. In the force ranges of 7–70 N and 75–110 N, T and F are quasi-linearly related (Figure 6i). Hence, we implement linear fitting to fit the data and obtain a sensitivity of 0.174 mV/N and -0.763 mV/N in the 7–70 N and 75–110 N force ranges, respectively. Although F and T do not have a one-to-one correspondence in the wearable T-THMI–nanophotonics system, all F 's can be distinguished by further analyzing their slopes. A positive slope suggests the force range of 7–70 N, while a negative slope indicates 75–110 N.

Toward practical applications, a smart glove is fabricated based on the wearable THMI–nanophotonics system for continuous real-time robotic control and VR/AR interactions. Recently, smart gloves as HMIs have two major advances. One is integrating numerous sensors on a single glove for accurate tactile sensing.⁸⁸ Enabled by the huge number of sensors, tactile sensing with great details can be achieved. Using deep learning methodology, the sensing information can reconstruct the hand motion exactly. The other direction is using a single glove for multivariant sensing, including temperature, strain, humidity, light, etc. In this way, the smart glove can mimic the complete human sensory system.⁸⁹ In comparison, our smart

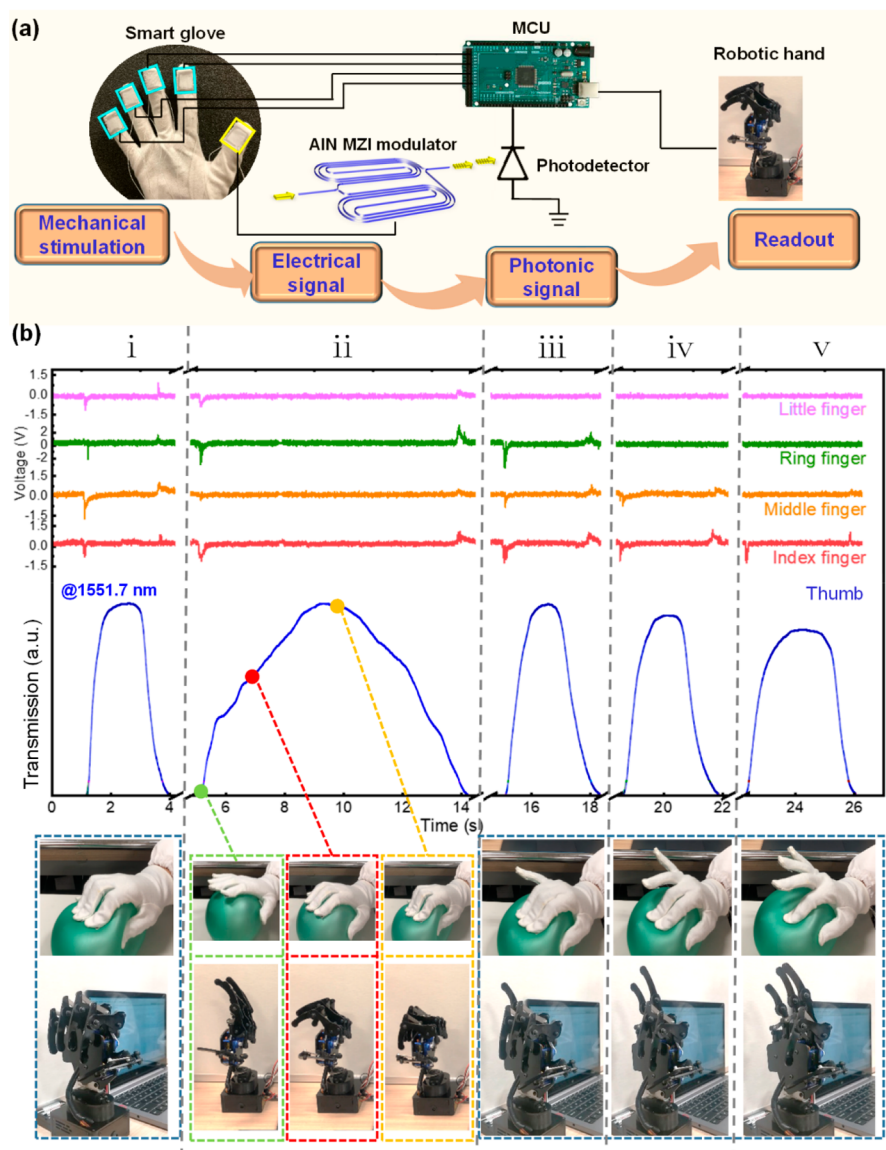


Figure 7. Demonstration of continuous real-time robotic hand control using the smart glove based on wearable THMI–nanophotonics systems. (a) Schematic circuit diagram of the robotic hand control system. (b) Optical signal output of the thumb and the corresponding signals of the other fingers for controlling the finger number and the movement speed of the robotic hand. Insets show photographs of the human hand and the robotic hand, respectively.

glove features self-sustainability and continuous real-time monitoring. Figure 7a illustrates the circuit diagram adopted in the robotic control application, as well as the physical quantities' transduction that allows the information flow. The information in the mechanical form is first converted into the electrical form *via* THMIs, then transforms into the photonic form by applying the electrical signal to AlN MZI modulators. Finally, the photonic readout is used for robotic hand control. Specifically, five individual sensors are knitted on five fingertips. Among them, only the thumb sensor is connected to the long AlN MZI modulator to achieve the open-circuit condition, and the generated photonic signal is converted to voltage by a photodetector, which is then connected to a microcontroller unit (MCU) for the analog-to-digital conversion. In addition, the other four fingers are directly connected to the MCU.

We demonstrate robotic hand control using different movement speeds and numbers of human fingers. As shown

in Figure 7b, when we pinch a balloon with the smart glove, pulse-like signals are generated at the moment of contact and separation for the index, middle, ring, and little finger, while the thumb signal shows continuous real-time changing curves related with F and v_F . Regarding conventional approaches of controlling robotic hands by THMIs, only two states, namely, grasping and releasing, can be achieved in one operation cycle due to the transient pulse-like signal without any intermediate state. However, in this demonstration, as shown in Figure 7b(ii), the robotic hand perfectly follows the movement of the human hand with the gradual grasping and releasing process. The insets show in detail three states during the process, including the zero- F (green box), the medium- F (red box), and the maximum- F (yellow box) states. On top of the continuous real-time control, the number of fingers can be manipulated. As shown in Figure 7b(i, iii, iv, and v), when we pinch and release the balloon using various numbers of fingers, the signals in each finger channel exhibit that the robotic hand responds with

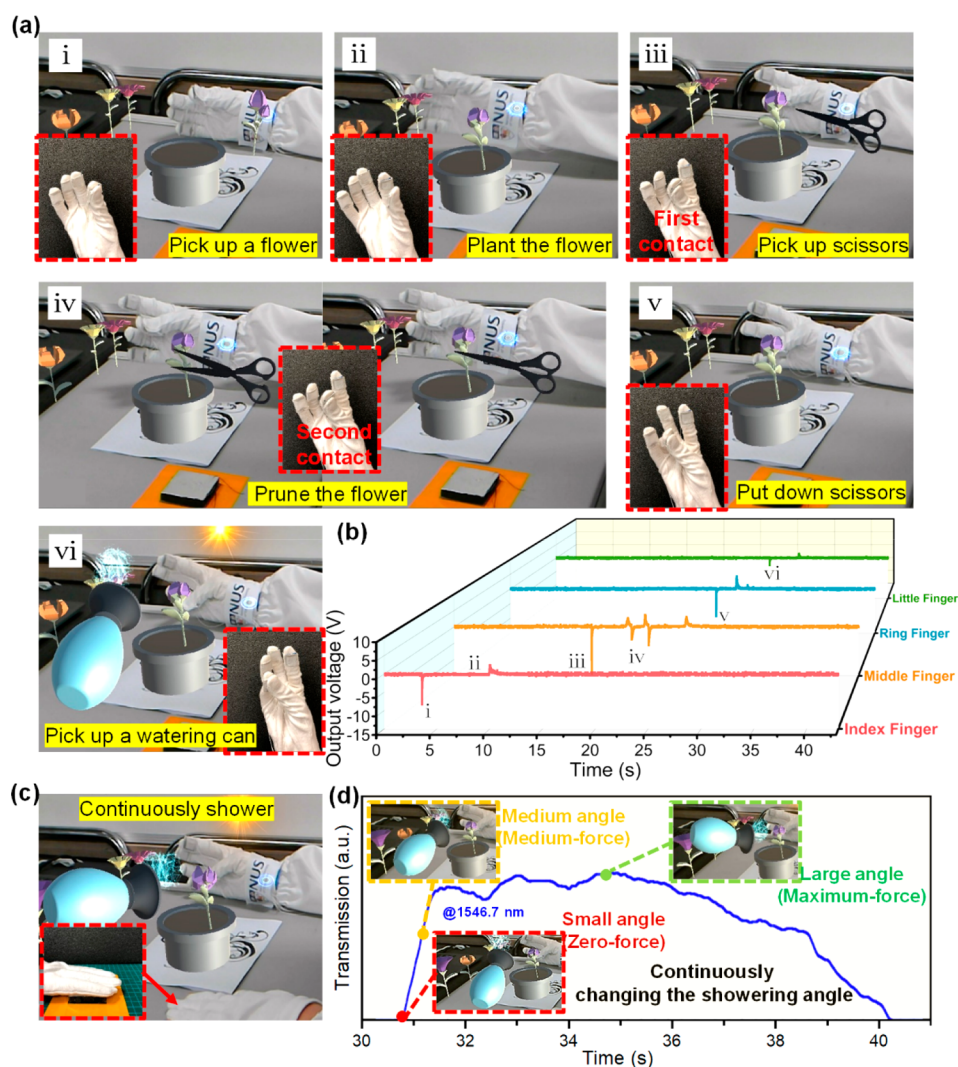


Figure 8. Demonstration of flower planting in the AR space based on the smart glove and the THMI–nanophotonics systems. (a) Screenshots of the flower planting process in the AR space. Insets show the corresponding gestures in each step. (b) Output signals of fingers in the flower planting process. (c) Screenshot of continuous watering of the flower in the AR space. Inset shows pressing the S-THMI with nanophotonic readout. (d) Curve of optical output in the continuous watering step. Insets show that the three watering angles can be controlled by different F 's.

the same fingers and v_F as the human hand. The corresponding video of the continuous real-time robotic hand control can be found in [Movie S3](#).

In AR applications that combine the real and the virtual world, enhancing natural environments and offering perceptually enriched experiences, real-time interactions are highly required with the least information loss from the real world. Thus, taking advantage of the excellent sensitivity, high temporal resolution, and self-sustainability of this proposed wearable THMI–nanophotonics system, we demonstrate a flower planting process in AR space. The corresponding circuit diagram is similar to [Figure 7a](#) and is presented in [Note S8](#). As demonstrated in [Figure 8a](#), with the smart gloves worn, discrete actions in the AR flower planting process are defined by different gestures. First, a flower is picked up when the index finger is contacted (i). Then, the separation between the index finger and the thumb commands planting the flower in the flowerpot (ii). Subsequently, by contacting the middle finger, scissors are picked up (iii). And with one more contact of the middle finger, the flower is pruned (iv). It should be

mentioned that the flower can be pruned multiple times as long as we contact the middle finger. Afterward, once the ring finger is contacted, the scissors are put down (v). Lastly, a watering can and sunshine appear when contacting the little finger (vi). [Figure 8b](#) shows the corresponding electrical output signals of the four fingers in each step. Subsequently, the continuous real-time control capability is leveraged in the watering step ([Figure 8c](#)). The watering angle of the can be adjusted in response to the states of the S-THMI upon pressing. [Figure 8d](#) shows the continuous real-time changing curve of the photonic signal during the pressing process, and three specific watering angles under three pressing states with different F 's are displayed in the insets. Some fluctuations are observed during the control. We attribute the fluctuations to the human force change instead of to the dissipation of electrons to the humid environment. As shown in [Figure 5c](#) to [g](#), in region I, the output voltage and the transmission do not vary at zero-force, suggesting negligible dissipation of electrons to the humid environment. A detailed video of this flowering planting process in the AR space can be found in [Movie S4](#).

CONCLUSION

In summary, to address the issue of the unstable and information-lossy pulse-like signals generated from self-sustainable THMIs, we leverage nanophotonic readout to suppress electrical state shifts. The triboelectric voltage caused by mechanical stimulations is applied to a micro parallel-plate capacitor sandwiching an AlN MZI to induce photonic readouts through the electro-optic Pockels effect. Thanks to the high-speed data transmission capability of nanophotonics, the wearable THMIs–nanophotonics system can achieve a temporal resolution of 1 μ s, which enables real-time monitoring. Integrating an S-THMI with a short 2.16 mm long AlN MZI modulator, a linear force sensitivity of 0.659 mV/N is achieved in the range of 35–60 N. In order to increase the applicable interaction force range, we leverage the broad material availability of triboelectric technology and fabricate a T-THMI. Using a longer 28.06 mm AlN MZI modulator with a higher voltage sensitivity, the interaction force range is extended to cover 7–110 N with a linear sensitivity of 0.174 mV/N in 7–70 N and -0.763 mV/N in 75–110 N. Notably, the linear force sensitivities are independent of force speeds, providing an indispensably good property for practical applications. Toward practical applications, we develop a smart glove based on the THMI–nanophotonics system and demonstrate continuous real-time robotics control and VR/AR interactions, illustrating the stable, continuous real-time, and information-lossless features. It is noteworthy that the demonstrated integrated system is not limited to the specified THMIs shown in this paper, but applicable generally to all sensors that rely on the triboelectrification and electrostatic induction mechanisms. The proposed wearable THMI–nanophotonics system provides a versatile solution for self-sustainable wearable devices for HMI applications.

METHODS

Fabrication of THMIs. For S-THMI, PTFE was utilized as the negative triboelectric material, while aluminum foil served as the positive triboelectric material and electrode material. We utilized PET as the substrate of S-THMI. A thin foam and a sponge were utilized as the spacer and the stage, respectively. It should be noted that the foam here acted as the stage to ensure the contact of two triboelectric layers because simply pressing the sponge was unable to ensure contact. The surface areas of substrates are 5×5 cm², and those of the inner stages, electrode materials, and triboelectric materials are 3×3 cm². The thickness of the fabricated S-THMI is 1 cm in total. First, two thin foams were attached individually to two PET substrates in the middle, followed by attaching an aluminum foil to the other side of each foam. Subsequently, we attached a PTFE film to one of the aluminum foil surfaces. Lastly, two substrates were assembled in parallel. In between, four sponge strips were arranged on the four edges as the spacer, where the PTFE layer and the aluminum foil layer were positioned face to face. An S-THMI could be obtained then.

For the T-THMI, we utilized Ecoflex and nitrile films as the triboelectric materials, carbon cloth as the electrode material, foam as the spacer, and textile as the sealing material for the whole device. The surface area of this fabricated sensor is 1.5×1.5 cm², and the whole thickness is about 3 mm. First, an Ecoflex solution was prepared by mixing components A and B in 1:1 weight ratio. Then, it was uniformly blade-coated on one piece of carbon cloth. After solidifying, a negative triboelectric layer was obtained. Meanwhile, a nitrile film was attached to one side of another piece of carbon cloth as the positive triboelectric layer. Subsequently, the Ecoflex and the nitrile layer were assembled face to face and in parallel with four foam strips in between as the spacer, which were arranged over the four edges of

the two layers. Then, two textile pieces were attached individually to the other side of both carbon cloths for insulation and sealing. Lastly, with threads sewing the four edges of the device to enhance the attachment between layers, a T-THMI could be obtained.

Fabrication of AlN MZI Modulators. The AlN MZI modulator fabrication started from a commercially available 8 in. Si wafer insulated by a thin layer of SiO₂. The bottom electrode was formed by a 120 nm TiN layer and a 50 nm Si₃N₄ layer. Then the bottom electrode was covered by a planarized 2 μ m SiO₂ layer for insulation. The 2 μ m SiO₂ layer also served as the bottom cladding for light confinement in the AlN waveguide. Next, a layer of 400 nm AlN was deposited, after which a 200 nm SiO₂ layer was deposited and patterned as the hard mask for AlN etching. After the formation of AlN waveguide patterns, another 2 μ m planarized SiO₂ layer was deposited as the upper cladding. Contact holes were opened followed by a 2 μ m Al layer deposition and patterning for bottom electrode contacts and top electrode formation.

Characterization of THMI. A force gauge system (Mecmesin Multitest 2.5-i test system) was utilized to apply forces with different magnitudes and speeds on the triboelectric sensors and enable a contact and separation process of the two triboelectric layers. A programmable electrometer (Keithley 6514) was utilized to test the open-circuit voltage, and an oscilloscope (Agilent DSO-X3034A) was connected to it for real-time data acquisition.

Characterization of AlN MZI Modulators. A tunable laser source (Keysight, 81960A tunable laser) was utilized to emit light, covering 1520 to 1610 nm with the minimum tuning step of 0.1 pm. The light was guided through a single-mode-maintaining polarization controller, then focused to the inverted tapered waveguide by a tapered fiber (OZ Optics, TSMJ-3A-1550-9/125-0.25-18-2.5-14-3-AR), and finally guided to AlN MZI modulators. The voltage was applied to the AlN MZI modulators through a GSG probe with a 100 μ m pitch (MPI, T26A GSG100). In the DC tuning characterization, a tunable DC voltage supply (Agilent, E3631A) was amplified by 20 times using a voltage amplifier (FLC Electronics, A400DI) before being connected to the GSG probe. A power meter (Keysight, 81636B power sensor), synchronized with the tunable laser source, was utilized for measuring the optical wavelength spectrum from the AlN MZI modulators. For the AC modulation, a waveform generator (HP, 33120A) was used as the power supply, whose voltage was also amplified by 20 times before being connected to the GSG probe. The modulated optical signals are amplified by an erbium-doped fiber amplifier (Thorlabs, EDFA100S) before being captured by a high-speed photodetector (Thorlabs, DET08CFC/M) and converted into RF output, which was then captured by an oscilloscope (Agilent Technologies, DSO93004L).

Characterization of Wearable THMI–Nanophotonics Systems. The general characterization is similar to that of the AlN MZI modulators and triboelectric sensors. The differences are as follows. First, the voltage applied on the AlN MZI modulators was provided by connecting the GSG probe with triboelectric sensors. Second, for the demonstration part, the contact and separation process was controlled by a human hand instead of the force gauge.

ASSOCIATED CONTENT

Supporting Information

The Supporting Information is available free of charge at <https://pubs.acs.org/doi/10.1021/acsnano.0c03728>.

General working mechanism of the integrated system, optical and tunneling electron microscope images of triboelectric–human–machine interfaces (THMIs) and nanophotonic readout circuits, output power fitting of the THMIs, sophisticated interferogram fitting method, AlN Mach–Zehnder interferometer direct current phase modulation analysis, analysis of overshoot in Figure 4g, derivation of the relationship between transmission and force in the wearable THMI–nanophotonics systems,

circuit diagram adopted in the augmented reality application (PDF)

Movie S1. Continuous real-time control of the speed of a wireless electronic toy car in real space (MP4)

Movie S2. Continuous real-time control of the acceleration of a drone in virtual reality space (MP4)

Movie S3. Continuous real-time control of a robotic hand with varying movement speeds and number of fingers (MP4)

Movie S4. Flower planting in augmented reality space (MP4)

AUTHOR INFORMATION

Corresponding Author

Chengkuo Lee – Department of Electrical and Computer Engineering, Center for Intelligent Sensors and MEMS (CISM), and NUS Graduate School for Integrative Sciences & Engineering (NGS), National University of Singapore, Singapore 117576 Singapore; orcid.org/0000-0002-8886-3649; Email: elelc@nus.edu.sg

Authors

Bowei Dong – Department of Electrical and Computer Engineering and Center for Intelligent Sensors and MEMS (CISM), National University of Singapore, Singapore 117576 Singapore

Yanqin Yang – Department of Electrical and Computer Engineering and Center for Intelligent Sensors and MEMS (CISM), National University of Singapore, Singapore 117576 Singapore

Qiongfeng Shi – Department of Electrical and Computer Engineering and Center for Intelligent Sensors and MEMS (CISM), National University of Singapore, Singapore 117576 Singapore

Siyu Xu – Department of Electrical and Computer Engineering and Center for Intelligent Sensors and MEMS (CISM), National University of Singapore, Singapore 117576 Singapore

Zhongda Sun – Department of Electrical and Computer Engineering and Center for Intelligent Sensors and MEMS (CISM), National University of Singapore, Singapore 117576 Singapore

Shiyang Zhu – Institute of Microelectronics, Agency for Science, Technology and Research (A*STAR), Singapore 138634 Singapore

Zixuan Zhang – Department of Electrical and Computer Engineering and Center for Intelligent Sensors and MEMS (CISM), National University of Singapore, Singapore 117576 Singapore

Dim-Lee Kwong – Institute of Microelectronics, Agency for Science, Technology and Research (A*STAR), Singapore 138634 Singapore

Guangya Zhou – Center for Intelligent Sensors and MEMS (CISM) and Department of Mechanical Engineering, National University of Singapore, Singapore 117608 Singapore

Kah-Wee Ang – Department of Electrical and Computer Engineering and Center for Intelligent Sensors and MEMS (CISM), National University of Singapore, Singapore 117576 Singapore; orcid.org/0000-0003-1919-3351

Complete contact information is available at: <https://pubs.acs.org/10.1021/acsnano.0c03728>

Author Contributions

#B. Dong, Y. Yang, and Q. Shi contributed equally to this work.

Notes

The authors declare no competing financial interest.

ACKNOWLEDGMENTS

This work was supported by the research grant CRP-15th (NRF-CRP15-2015-02) “Piezoelectric Photonics Using CMOS Compatible AlN Technology for Enabling the Next Generation Photonics ICs and Nanosensors” at the National University of Singapore (NUS), Singapore; the A*STAR-NCBR research grant “Chip-Scale MEMS Micro-Spectrometer for Monitoring Harsh Industrial Gases” (R-263-000-C91-305) at the NUS, Singapore; the RIE Advanced Manufacturing and Engineering (AME) programmatic grant A18A4b0055 “Nanosystems at the Edge” at NUS, Singapore; and the National Research Foundation Singapore under its AI Singapore Programme (Award Number AISG-GC-2019-002).

REFERENCES

- (1) Kim, J.; Campbell, A. S.; de Ávila, B. E. F.; Wang, J. Wearable Biosensors for Healthcare Monitoring. *Nat. Biotechnol.* **2019**, *37*, 389–406.
- (2) Yang, Y.; Gao, W. Wearable and Flexible Electronics for Continuous Molecular Monitoring. *Chem. Soc. Rev.* **2019**, *48*, 1465–1491.
- (3) Wang, C.; Hwang, D.; Yu, Z.; Takei, K.; Park, J.; Chen, T.; Ma, B.; Javey, A. User-Interactive Electronic Skin for Instantaneous Pressure Visualization. *Nat. Mater.* **2013**, *12*, 899–904.
- (4) Wu, Y.; Mechael, S. S.; Lerma, C.; Carmichael, R. S.; Carmichael, T. B. Stretchable Ultrasheer Fabrics as Semitransparent Electrodes for Wearable Light-Emitting e-Textiles with Changeable Display Patterns. *Matter* **2020**, *2*, 882–895.
- (5) Yang, J. C.; Mun, J.; Kwon, S. Y.; Park, S.; Bao, Z.; Park, S. Electronic Skin: Recent Progress and Future Prospects for Skin-Attachable Devices for Health Monitoring, Robotics, and Prosthetics. *Adv. Mater.* **2019**, *31*, 1904765.
- (6) Kim, Y.; Chortos, A.; Xu, W.; Liu, Y.; Oh, J. Y.; Son, D.; Kang, J.; Foudeh, A. M.; Zhu, C.; Lee, Y.; Niu, S.; Liu, J.; Pfattner, R.; Bao, Z.; Lee, T. W. A Bioinspired Flexible Organic Artificial Afferent Nerve. *Science* **2018**, *360*, 998–1003.
- (7) He, T.; Wang, H.; Wang, J.; Tian, X.; Wen, F.; Shi, Q.; Ho, J. S.; Lee, C. Self-Sustainable Wearable Textile Nano-Energy Nano-System (NENS) for Next-Generation Healthcare Applications. *Adv. Sci.* **2019**, *6*, 1901437.
- (8) Shi, Q.; He, T.; Lee, C. More than Energy Harvesting - Combining Triboelectric Nanogenerator and Flexible Electronics Technology for Enabling Novel Micro-/Nano-Systems. *Nano Energy* **2019**, *57*, 851–871.
- (9) Bai, W.; Yang, H.; Ma, Y.; Chen, H.; Shin, J.; Liu, Y.; Yang, Q.; Kandela, I.; Liu, Z.; Kang, S. K.; Wei, C.; Haney, C. R.; Brikha, A.; Ge, X.; Feng, X.; Braun, P. V.; Huang, Y.; Zhou, W.; Rogers, J. A. Flexible Transient Optical Waveguides and Surface-Wave Biosensors Constructed from Monocrystalline Silicon. *Adv. Mater.* **2018**, *30*, 1801584.
- (10) Bamiedakis, N.; Shi, F.; Chu, D.; Penty, R. V.; White, I. H. High-Speed Data Transmission over Flexible Multimode Polymer Waveguides under Flexure. *IEEE Photonics Technol. Lett.* **2018**, *30*, 1329–1332.
- (11) Larson, C.; Peele, B.; Li, S.; Robinson, S.; Totaro, M.; Beccai, L.; Mazzolai, B.; Shepherd, R. Highly Stretchable Electroluminescent Skin for Optical Signaling and Tactile Sensing. *Science* **2016**, *351*, 1071–1074.
- (12) Bariya, M.; Nyein, H. Y. Y.; Javey, A. Wearable Sweat Sensors. *Nat. Electron.* **2018**, *1*, 160–171.
- (13) Song, Y. M.; Xie, Y.; Malyarchuk, V.; Xiao, J.; Jung, I.; Choi, K. J.; Liu, Z.; Park, H.; Lu, C.; Kim, R. H.; Li, R.; Crozier, K. B.; Huang,

- Y.; Rogers, J. A. Digital Cameras with Designs Inspired by the Arthropod Eye. *Nature* **2013**, *497*, 95–99.
- (14) Liu, H.; Lu, Z.; Zhang, Z.; Wang, Y.; Zhang, H. Highly Elastic Organic Crystals for Flexible Optical Waveguides. *Angew. Chem., Int. Ed.* **2018**, *57*, 8448–8452.
- (15) Torres Alonso, E.; Rodrigues, D. P.; Khetani, M.; Shin, D.-W.; De Sanctis, A.; Joulie, H.; de Schrijver, I.; Baldycheva, A.; Alves, H.; Neves, A. I. S.; Russo, S.; Craciun, M. F. Graphene Electronic Fibres with Touch-Sensing and Light-Emitting Functionalities for Smart Textiles. *npj Flex. Electron.* **2018**, *2*, 25.
- (16) Karl, M.; Glackin, J. M. E.; Schubert, M.; Kronenberg, N. M.; Turnbull, G. A.; Samuel, I. D. W.; Gather, M. C. Flexible and Ultra-Lightweight Polymer Membrane Lasers. *Nat. Commun.* **2018**, *9*, 1525.
- (17) Li, L.; Hongtao, L.; Yizhong, H.; Ren-Jye, S.; Yadav, A.; Junying, L.; Michon, J.; Englund, D.; Richardson, K.; Gu, T.; Hu, J. High-Performance Flexible Waveguide-Integrated Photodetectors. *Optica* **2018**, *5*, 44–51.
- (18) Lee, S.; Shi, Q.; Lee, C. From Flexible Electronics Technology in the Era of IoT and Artificial Intelligence toward Future Implanted Body Sensor Networks. *APL Mater.* **2019**, *7*, 031302.
- (19) Li, S.; Ni, Q.; Sun, Y.; Min, G.; Al-Rubaye, S. Energy-Efficient Resource Allocation for Industrial Cyber-Physical IoT Systems in 5G Era. *IEEE Trans. Ind. Informatics* **2018**, *14*, 2618–2628.
- (20) Niu, S.; Matsuhisa, N.; Beker, L.; Li, J.; Wang, S.; Wang, J.; Jiang, Y.; Yan, X.; Yun, Y.; Burnett, W.; Poon, A. S. Y.; Tok, J. B.-H.; Chen, X.; Bao, Z. A Wireless Body Area Sensor Network Based on Stretchable Passive Tags. *Nat. Electron.* **2019**, *2*, 361–368.
- (21) Wang, Z. L.; Chen, J.; Lin, L. Progress in Triboelectric Nanogenerators as a New Energy Technology and Self-Powered Sensors. *Energy Environ. Sci.* **2015**, *8*, 2250–2282.
- (22) Luo, J.; Wang, Z. L. Recent Advances in Triboelectric Nanogenerator Based Self-Charging Power Systems. *Energy Storage Mater.* **2019**, *23*, 617–628.
- (23) Shi, B.; Liu, Z.; Zheng, Q.; Meng, J.; Ouyang, H.; Zou, Y.; Jiang, D.; Qu, X.; Yu, M.; Zhao, L.; Fan, Y.; Wang, Z. L.; Li, Z. Body-Integrated Self-Powered System for Wearable and Implantable Applications. *ACS Nano* **2019**, *13*, 6017–6024.
- (24) Park, S. J.; Lee, S. H.; Seol, M. L.; Jeon, S. B.; Bae, H.; Kim, D.; Cho, G. H.; Choi, Y. K. Self-Sustainable Wind Speed Sensor System with Omni-Directional Wind Based Triboelectric Generator. *Nano Energy* **2019**, *55*, 115–122.
- (25) Nozariasmarz, A.; Collins, H.; Dsouza, K.; Polash, M. H.; Hosseini, M.; Hyland, M.; Liu, J.; Malhotra, A.; Ortiz, F. M.; Mohaddes, F.; Ramesh, V. P.; Sargolzaeiaval, Y.; Snouwaert, N.; Özturk, M. C.; Vashae, D. Review of Wearable Thermoelectric Energy Harvesting: From Body Temperature to Electronic Systems. *Appl. Energy* **2020**, *258*, 114069.
- (26) Zhang, Y.; Peng, M.; Liu, Y.; Zhang, T.; Zhu, Q.; Lei, H.; Liu, S.; Tao, Y.; Li, L.; Wen, Z.; Sun, X. Flexible Self-Powered Real-Time Ultraviolet Photodetector by Coupling Triboelectric and Photoelectric Effects. *ACS Appl. Mater. Interfaces* **2020**, *12*, 19384–19392.
- (27) Wen, Z.; Fu, J.; Han, L.; Liu, Y.; Peng, M.; Zheng, L.; Zhu, Y.; Sun, X.; Zi, Y. Toward Self-Powered Photodetection Enabled by Triboelectric Nanogenerators. *J. Mater. Chem. C* **2018**, *6*, 11893–11902.
- (28) Zhang, C.; Zhang, Z. H.; Yang, X.; Zhou, T.; Han, C. B.; Wang, Z. L. Tribotronic Phototransistor for Enhanced Photodetection and Hybrid Energy Harvesting. *Adv. Funct. Mater.* **2016**, *26*, 2554–2560.
- (29) Zou, Y.; Tan, P.; Shi, B.; Ouyang, H.; Jiang, D.; Liu, Z.; Li, H.; Yu, M.; Wang, C.; Qu, X.; Zhao, L.; Fan, Y.; Wang, Z. L.; Li, Z. A Bionic Stretchable Nanogenerator for Underwater Sensing and Energy Harvesting. *Nat. Commun.* **2019**, *10*, 2695.
- (30) Jiang, D.; Ouyang, H.; Shi, B.; Zou, Y.; Tan, P.; Qu, X.; Chao, S.; Xi, Y.; Zhao, C.; Fan, Y.; Li, Z. A Wearable Noncontact Free-Rotating Hybrid Nanogenerator for Self-Powered Electronics. *InfoMater.* **2020**, DOI: 10.1002/inf2.12103.
- (31) Tan, P.; Zheng, Q.; Zou, Y.; Shi, B.; Jiang, D.; Qu, X.; Ouyang, H.; Zhao, C.; Cao, Y.; Fan, Y.; Wang, Z. L.; Li, Z. A Battery-Like Self-Charge Universal Module for Motional Energy Harvest. *Adv. Energy Mater.* **2019**, *9*, 1901875.
- (32) Su, L.; Wang, H.; Tian, Z.; Wang, H.; Cheng, Q.; Yu, W. Low Detection Limit and High Sensitivity Wind Speed Sensor Based on Triboelectrification-Induced Electroluminescence. *Adv. Sci.* **2019**, *6*, 1901980.
- (33) Sun, J.; Yang, A.; Zhao, C.; Liu, F.; Li, Z. Recent Progress of Nanogenerators Acting as Biomedical Sensors *In Vivo*. *Sci. Bull.* **2019**, *64*, 1336–1347.
- (34) Dong, K.; Wang, Y. C.; Deng, J.; Dai, Y.; Zhang, S. L.; Zou, H.; Gu, B.; Sun, B.; Wang, Z. L. A Highly Stretchable and Washable All-Yarn-Based Self-Charging Knitting Power Textile Composed of Fiber Triboelectric Nanogenerators and Supercapacitors. *ACS Nano* **2017**, *11*, 9490–9499.
- (35) Lv, J.; Jeerapan, I.; Tehrani, F.; Yin, L.; Silva-Lopez, C. A.; Jang, J. H.; Joshua, D.; Shah, R.; Liang, Y.; Xie, L.; Soto, F.; Chen, C.; Karshalev, E.; Kong, C.; Yang, Z.; Wang, J. Sweat-Based Wearable Energy Harvesting-Storage Hybrid Textile Devices. *Energy Environ. Sci.* **2018**, *11*, 3431–3442.
- (36) Wang, D.; Yuan, G.; Hao, G.; Wang, Y. All-Inorganic Flexible Piezoelectric Energy Harvester Enabled by Two-Dimensional Mica. *Nano Energy* **2018**, *43*, 351–358.
- (37) Hou, C.; Chen, T.; Li, Y.; Huang, M.; Shi, Q.; Liu, H.; Sun, L.; Lee, C. A Rotational Pendulum Based Electromagnetic/Triboelectric Hybrid-Generator for Ultra-Low-Frequency Vibrations Aiming at Human Motion and Blue Energy Applications. *Nano Energy* **2019**, *63*, 103871.
- (38) Pu, X.; Song, W.; Liu, M.; Sun, C.; Du, C.; Jiang, C.; Huang, X.; Zou, D.; Hu, W.; Wang, Z. L. Wearable Power-Textiles by Integrating Fabric Triboelectric Nanogenerators and Fiber-Shaped Dye-Sensitized Solar Cells. *Adv. Energy Mater.* **2016**, *6*, 1601048.
- (39) Yang, Y.; Sun, N.; Wen, Z.; Cheng, P.; Zheng, H.; Shao, H.; Xia, Y.; Chen, C.; Lan, H.; Xie, X.; Zhou, C.; Zhong, J.; Sun, X.; Lee, S. T. Liquid-Metal-Based Super-Stretchable and Structure-Designable Triboelectric Nanogenerator for Wearable Electronics. *ACS Nano* **2018**, *12*, 2027–2034.
- (40) Lee, K. Y.; Yoon, H. J.; Jiang, T.; Wen, X.; Seung, W.; Kim, S. W.; Wang, Z. L. Fully Packaged Self-Powered Triboelectric Pressure Sensor Using Hemispheres-Array. *Adv. Energy Mater.* **2016**, *6*, 1502566.
- (41) Sun, C.; Shi, Q.; Hasan, D.; Yazici, M. S.; Zhu, M.; Ma, Y.; Dong, B.; Liu, Y.; Lee, C. Self-Powered Multifunctional Monitoring System Using Hybrid Integrated Triboelectric Nanogenerators and Piezoelectric Microsensors. *Nano Energy* **2019**, *58*, 612–623.
- (42) Guo, Y.; Zhang, X. S.; Wang, Y.; Gong, W.; Zhang, Q.; Wang, H.; Brugger, J. All-Fiber Hybrid Piezoelectric-Enhanced Triboelectric Nanogenerator for Wearable Gesture Monitoring. *Nano Energy* **2018**, *48*, 152–160.
- (43) Song, K.; Zhao, R.; Wang, Z. L.; Yang, Y. Conjoined Pyro-Piezoelectric Effect for Self-Powered Simultaneous Temperature and Pressure Sensing. *Adv. Mater.* **2019**, *31*, 1802831.
- (44) Wang, C.; Li, X.; Hu, H.; Zhang, L.; Huang, Z.; Lin, M.; Zhang, Z.; Yin, Z.; Huang, B.; Gong, H.; Bhaskaran, S.; Gu, Y.; Makihata, M.; Guo, Y.; Lei, Y.; Chen, Y.; Wang, C.; Li, Y.; Zhang, T.; Chen, Z.; et al. Monitoring of the Central Blood Pressure Waveform via a Conformal Ultrasonic Device. *Nat. Biomed. Eng.* **2018**, *2*, 687–695.
- (45) Liang, X.; Jiang, T.; Liu, G.; Feng, Y.; Zhang, C.; Wang, Z. L. Spherical Triboelectric Nanogenerator Integrated with Power Management Module for Harvesting Multidirectional Water Wave Energy. *Energy Environ. Sci.* **2020**, *13*, 277–285.
- (46) Chen, Y.; Cheng, Y.; Jie, Y.; Cao, X.; Wang, N.; Wang, Z. L. Energy Harvesting and Wireless Power Transmission by a Hybridized Electromagnetic-Triboelectric Nanogenerator. *Energy Environ. Sci.* **2019**, *12*, 2678–2684.
- (47) Jeon, S. B.; Park, S. J.; Kim, W. G.; Tcho, I. W.; Jin, I. K.; Han, J. K.; Kim, D.; Choi, Y. K. Self-Powered Wearable Keyboard with Fabric Based Triboelectric Nanogenerator. *Nano Energy* **2018**, *53*, 596–603.

- (48) Seol, M. L.; Jeon, S. B.; Han, J. W.; Choi, Y. K. Ferrofluid-Based Triboelectric-Electromagnetic Hybrid Generator for Sensitive and Sustainable Vibration Energy Harvesting. *Nano Energy* **2017**, *31*, 233–238.
- (49) Shin, Y. E.; Lee, J. E.; Park, Y.; Hwang, S. H.; Chae, H. G.; Ko, H. Sewing Machine Stitching of Polyvinylidene Fluoride Fibers: Programmable Textile Patterns for Wearable Triboelectric Sensors. *J. Mater. Chem. A* **2018**, *6*, 22879–22888.
- (50) Kim, I.; Roh, H.; Kim, D. Willow-like Portable Triboelectric Respiration Sensor Based on Polyethylenimine-Assisted CO₂ Capture. *Nano Energy* **2019**, *65*, 103990.
- (51) Bhatia, D.; Lee, J.; Hwang, H. J.; Baik, J. M.; Kim, S.; Choi, D. Design of Mechanical Frequency Regulator for Predictable Uniform Power from Triboelectric Nanogenerators. *Adv. Energy Mater.* **2018**, *8*, 1702667.
- (52) Fan, F. R.; Tian, Z. Q.; Lin Wang, Z. Flexible Triboelectric Generator. *Nano Energy* **2012**, *1*, 328–334.
- (53) Lim, K. W.; Peddigari, M.; Park, C. H.; Lee, H. Y.; Min, Y.; Kim, J. W.; Ahn, C. W.; Choi, J. J.; Hahn, B. D.; Choi, J. H.; Park, D. S.; Hong, J. K.; Yeom, J. T.; Yoon, W. H.; Ryu, J.; Yi, S. N.; Hwang, G. T. A High Output Magneto-Mechano-Triboelectric Generator Enabled by Accelerated Water-Soluble Nano-Bullets for Powering a Wireless Indoor Positioning System. *Energy Environ. Sci.* **2019**, *12*, 666–674.
- (54) Ha, M.; Lim, S.; Cho, S.; Lee, Y.; Na, S.; Baig, C.; Ko, H. Skin-Inspired Hierarchical Polymer Architectures with Gradient Stiffness for Spacer-Free, Ultrathin, and Highly Sensitive Triboelectric Sensors. *ACS Nano* **2018**, *12*, 3964–3974.
- (55) Dudem, B.; Huynh, N. D.; Kim, W.; Kim, D. H.; Hwang, H. J.; Choi, D.; Yu, J. S. Nanopillar-Array Architected PDMS-Based Triboelectric Nanogenerator Integrated with a Windmill Model for Effective Wind Energy Harvesting. *Nano Energy* **2017**, *42*, 269–281.
- (56) Chung, J.; Heo, D.; Shin, G.; Choi, D.; Choi, K.; Kim, D.; Lee, S. Ion-Enhanced Field Emission Triboelectric Nanogenerator. *Adv. Energy Mater.* **2019**, *9*, 1901731.
- (57) Hinchet, R.; Yoon, H.-J.; Ryu, H.; Kim, M.-K.; Choi, E.-K.; Kim, D.-S.; Kim, S.-W. Transcutaneous Ultrasound Energy Harvesting Using Capacitive Triboelectric Technology. *Science* **2019**, *365*, 491–494.
- (58) Choi, W.; Yun, I.; Jeung, J.; Park, Y. S.; Cho, S.; Kim, D. W.; Kang, I. S.; Chung, Y.; Jeong, U. Stretchable Triboelectric Multimodal Tactile Interface Simultaneously Recognizing Various Dynamic Body Motions. *Nano Energy* **2019**, *56*, 347–356.
- (59) Seo, B.; Cha, Y.; Kim, S.; Choi, W. Rational Design for Optimizing Hybrid Thermo-Triboelectric Generators Targeting Human Activities. *ACS Energy Lett.* **2019**, *4*, 2069–2074.
- (60) Wang, Z. L.; Wang, A. C. On the Origin of Contact-Electrification. *Mater. Today* **2019**, *30*, 34–51.
- (61) Wang, Z. L. On the First Principle Theory of Nanogenerators from Maxwell's Equations. *Nano Energy* **2020**, *68*, 104272.
- (62) Wu, C.; Wang, A. C.; Ding, W.; Guo, H.; Wang, Z. L. Triboelectric Nanogenerator: A Foundation of the Energy for the New Era. *Adv. Energy Mater.* **2019**, *9*, 1802906.
- (63) Lee, J. H.; Hinchet, R.; Kim, S. K.; Kim, S.; Kim, S. W. Shape Memory Polymer-Based Self-Healing Triboelectric Nanogenerator. *Energy Environ. Sci.* **2015**, *8*, 3605–3613.
- (64) Parida, K.; Thangavel, G.; Cai, G.; Zhou, X.; Park, S.; Xiong, J.; Lee, P. S. Extremely Stretchable and Self-Healing Conductor Based on Thermoplastic Elastomer for All-Three-Dimensional Printed Triboelectric Nanogenerator. *Nat. Commun.* **2019**, *10*, 2158.
- (65) Šutka, A.; Malnieks, K.; Linarts, A.; Timusk, M.; Jurkāns, V.; Gorņevs, I.; Blums, J.; Berziņa, A.; Joost, U.; Knite, M. Inversely Polarised Ferroelectric Polymer Contact Electrodes for Triboelectric-like Generators from Identical Materials. *Energy Environ. Sci.* **2018**, *11*, 1437–1443.
- (66) Qiu, C.; Wu, F.; Lee, C.; Rasit, M. Nano Energy Self-Powered Control Interface Based on Gray Code with Hybrid Triboelectric and Photovoltaics Energy Harvesting for IoT Smart Home and Access Control Applications. *Nano Energy* **2020**, *70*, 104456.
- (67) Anaya, D. V.; He, T.; Lee, C.; Yuce, M. R. Self-Powered Eye Motion Sensor Based on Triboelectric Interaction and Near-Field Electrostatic Induction for Wearable Assistive Technologies. *Nano Energy* **2020**, *72*, 104675.
- (68) Shi, Q.; Lee, C. Self-Powered Bio-Inspired Spider-Net-Coding Interface Using Single-Electrode Triboelectric Nanogenerator. *Adv. Sci.* **2019**, *6*, 1900617.
- (69) Chen, T.; Shi, Q.; Zhu, M.; He, T.; Sun, L.; Yang, L.; Lee, C. Triboelectric Self-Powered Wearable Flexible Patch as 3D Motion Control Interface for Robotic Manipulator. *ACS Nano* **2018**, *12*, 11561–11571.
- (70) Chen, T.; Zhao, M.; Shi, Q.; Yang, Z.; Liu, H.; Sun, L.; Ouyang, J.; Lee, C. Novel Augmented Reality Interface Using a Self-Powered Triboelectric Based Virtual Reality 3D-Control Sensor. *Nano Energy* **2018**, *51*, 162–172.
- (71) Shi, Q.; Wang, H.; Wang, T.; Lee, C. Self-Powered Liquid Triboelectric Microfluidic Sensor for Pressure Sensing and Finger Motion Monitoring Applications. *Nano Energy* **2016**, *30*, 450–459.
- (72) He, T.; Sun, Z.; Shi, Q.; Zhu, M.; Anaya, D. V.; Xu, M.; Chen, T.; Yuce, M. R.; Thean, A. V. Y.; Lee, C. Self-Powered Glove-Based Intuitive Interface for Diversified Control Applications in Real/Cyber Space. *Nano Energy* **2019**, *58*, 641–651.
- (73) Yu, J.; Hou, X.; Cui, M.; Zhang, S.; He, J.; Geng, W.; Mu, J.; Chou, X. Highly Skin-Conformal Wearable Tactile Sensor Based on Piezoelectric-Enhanced Triboelectric Nanogenerator. *Nano Energy* **2019**, *64*, 103923.
- (74) Pu, X.; Guo, H.; Chen, J.; Wang, X.; Xi, Y.; Hu, C.; Wang, Z. L. Eye Motion Triggered Self-Powered Mechnosensational Communication System Using Triboelectric Nanogenerator. *Sci. Adv.* **2017**, *3*, No. e1700694.
- (75) Han, Y.; Yi, F.; Jiang, C.; Dai, K.; Xu, Y.; Wang, X.; You, Z. Self-Powered Gait Pattern-Based Identity Recognition by a Soft and Stretchable Triboelectric Band. *Nano Energy* **2019**, *56*, 516–523.
- (76) Guo, H.; Pu, X.; Chen, J.; Meng, Y.; Yeh, M.-H.; Liu, G.; Tang, Q.; Chen, B.; Liu, D.; Qi, S.; Wu, C.; Hu, C.; Wang, J.; Wang, Z. L. A Highly Sensitive, Self-Powered Triboelectric Auditory Sensor for Social Robotics and Hearing Aids. *Sci. Robot.* **2018**, *3*, No. eaat2516.
- (77) Zhang, B.; Tang, Y.; Dai, R.; Wang, H.; Sun, X.; Qin, C.; Pan, Z.; Liang, E.; Mao, Y. Breath-Based Human–Machine Interaction System Using Triboelectric Nanogenerator. *Nano Energy* **2019**, *64*, 103953.
- (78) Wen, F.; Wang, H.; He, T.; Shi, Q.; Sun, Z.; Zhu, M.; Zhang, Z.; Cao, Z.; Dai, Y.; Zhang, T.; Lee, C. Battery-Free Short-Range Self-Powered Wireless Sensor Network (SS-WSN) Using TENG Based Direct Sensory Transmission (TDST) Mechanism. *Nano Energy* **2020**, *67*, 104266.
- (79) Liu, S.; Wang, H.; He, T.; Dong, S.; Lee, C. Switchable Textile-Triboelectric Nanogenerators (S-TENGs) for Continuous Profile Sensing Application without Environmental Interferences. *Nano Energy* **2020**, *69*, 104462.
- (80) Wang, Z.; Liu, W.; Hu, J.; He, W.; Yang, H.; Ling, C.; Xi, Y.; Wang, X.; Liu, A.; Hu, C. Two Voltages in Contact-Separation Triboelectric Nanogenerator: From Asymmetry to Symmetry for Maximum Output. *Nano Energy* **2020**, *69*, 104452.
- (81) Wang, H.; Wu, H.; Hasan, D.; He, T.; Shi, Q.; Lee, C. Self-Powered Dual-Mode Amenity Sensor Based on the Water-Air Triboelectric Nanogenerator. *ACS Nano* **2017**, *11*, 10337–10346.
- (82) He, T.; Shi, Q.; Wang, H.; Wen, F.; Chen, T.; Ouyang, J.; Lee, C. Beyond Energy Harvesting - Multi-Functional Triboelectric Nanosensors on a Textile. *Nano Energy* **2019**, *57*, 338–352.
- (83) Wu, C.; Ding, W.; Liu, R.; Wang, J.; Wang, A. C.; Wang, J.; Li, S.; Zi, Y.; Wang, Z. L. Keystroke Dynamics Enabled Authentication and Identification Using Triboelectric Nanogenerator Array. *Mater. Today* **2018**, *21*, 216–222.
- (84) Zhao, G.; Yang, J.; Chen, J.; Zhu, G.; Jiang, Z.; Liu, X.; Niu, G.; Wang, Z. L.; Zhang, B. Keystroke Dynamics Identification Based on Triboelectric Nanogenerator for Intelligent Keyboard Using Deep Learning Method. *Adv. Mater. Technol.* **2019**, *4*, 1800167.

(85) Zhang, W.; Wang, P.; Sun, K.; Wang, C.; Diao, D. Intelligently Detecting and Identifying Liquids Leakage Combining Triboelectric Nanogenerator Based Self-Powered Sensor with Machine Learning. *Nano Energy* **2019**, *56*, 277–285.

(86) Zhu, M.; Sun, Z.; Zhang, Z.; Shi, Q.; He, T.; Liu, H.; Chen, T.; Lee, C. Haptic-Feedback Smart Glove as a Creative Human-Machine Interface (HMI) for Virtual/Augmented Reality Applications. *Sci. Adv.* **2020**, *6*, No. eaaz8693.

(87) Wen, F.; Sun, Z.; He, T.; Shi, Q.; Zhu, M.; Zhang, Z. Machine Learning Glove Using Self-Powered Conductive Superhydrophobic Triboelectric Textile for Gesture Recognition in VR/AR Applications. *Adv. Sci.* **2020**, *2000261*, 1–15.

(88) Sundaram, S.; Kellnhofer, P.; Li, Y.; Zhu, J.-Y.; Torralba, A.; Matusik, W. Learning the Signatures of the Human Grasp Using a Scalable Tactile Glove. *Nature* **2019**, *569*, 698–702.

(89) Hua, Q.; Sun, J.; Liu, H.; Bao, R.; Yu, R.; Zhai, J.; Pan, C.; Wang, Z. L. Skin-Inspired Highly Stretchable and Conformable Matrix Networks for Multifunctional Sensing. *Nat. Commun.* **2018**, *9*, 244.